Surface plasmon effects induced by uncollimated emission of semiconductor microstructures

Dominic Lepage and Jan J. Dubowski*
Department of Electrical and Computer Engineering, Center of Excellence for Information Engineering, Université de Sherbrooke, Sherbrooke, Québec J1K 2R1, Canada
** Corresponding author: www.dubowski.ca*

ABSTRACT

We investigate the functioning of an innovative monolithically integrated surface plasmon resonance (SPR) device comprising a metal coated SiO_2 layer deposited atop a photoluminescence emitting quantum well (QW) wafer. The device takes advantage of the uncollimated and incoherent emission of QW microstructure. This presents a non-trivial problem in our goal to describe quantitatively the functioning of such a device. We discuss the results of our calculations based on a rigorous coupled-wave analysis algorithm and tensorial approach aimed at the full description of surface plasmons (SPs) coupling in QW semiconductor-based SPR architectures designed for biosensing applications. The results indicate that the injected in-plane wavevectors increase the SPs coupling efficiency up to 10^3 times in comparison to indirect SPs injection. We discuss the general idea of an experimental setup required for collecting the 3D measurement of SPR dispersion relations $\hbar\omega(\mathbf{k_x},\mathbf{k_y})$, potentially enabling a much richer picture of surficial biochemical events. Preliminary results indicate that the proposed methodology produces simultaneously the equivalent of 10^5 to 10^8 conventional SPR scans achievable with commercial systems.

Keywords: Surface plasmon resonance, optical devices, light scattering, biosensing, hyperspectral imaging

1. INTRODUCTION

The inherent surface sensitivity of the surface plasmon resonance (SPR) effect has made it highly attractive for biochemical analysis of processes localized on metal surfaces. Many SPR apparatus have been developed and made commercially available for that purpose in the past 20 years[1], where they are widely employed in research and development. However, most of them are relatively bulky, expensive and hard to combine with other detection methods, preventing applications in more practical areas such as field biosensing. A monolithically integrated SPR microchip, which could be easily included in specimen processing hardware for a wholly automated analysis, has yet to be demonstrated. A first step towards this integration would be embedding a light source in a microstructure designed for SPR. Strong photoluminescence (PL) from some bulk semiconductor materials or their microstructures in form of thin films, quantum well (QW), quantum dot (QD), and arrays of nano-crystals (NCs) makes them attractive for the development of monolithically integrated SPR devices.

The incidence of an electromagnetic (EM) wave on a thin dielectric-metal-dielectric (DMD) microstructure, under certain conditions, will result in the coupling of the incoming wave with surface waves of the free electrons at the metal surface (an electro-optical wave). The occurrence of this phenomenon is denominated as SPR. The conditions of the resonance are highly dependent on the metal surficial properties (within ~200-nm), which could be perturbed by biochemical events and thus generate a biosensitive surface. Amongst other things, the SPR event is also dependent on the injected energy of the EM field, its polarization and polar angular incidence on the metal layer. All these are normally fixed by the manufacturer in commercial systems and the polar angles mechanically scanned.

A DMD microstructure deposited on top of a PL emitting semiconductor could provide conditions suitable for surface plasmons (SPs) formation and observation of a variety of bio-chemical reactions. Because of the proximity and the nature of the materials involved, the light injected in such a system is uncollimated and usually incoherent, as opposed to laser induced SPR. As illustrated in the inset of Fig. 1, any given point of a metallic layer in the DMD microstructure will be exposed to the whole wavevector spectrum k_{ll} (polar angles of emission) and couple all SPR modes possibly supported by the architecture for the excited energies. While a constant light intensity is measured at a given plane of the real-space, every supported photonic mode is induced in the Fourier-space (k_{ll}). Fig. 1 illustrates this principle by showing the distribution of the P-polarized electric field intensity for a vertical cross section (z) of such

Synthesis and Photonics of Nanoscale Materials VII, edited by Jan J. Dubowski, David B. Geohegan, Frank Träger,
Proc. of SPIE Vol. 7586, 758607 · © 2010 SPIE · CCC code: 0277-786X/10/$18 · doi: 10.1117/12.843239

Downloaded from SPIE Digital Library on 17 Jun 2010 to 132.210.72.142. Terms of Use: http://spiedl.org/terms

architecture at the various wavevectors (k_{ll}) emitted by an embedded QW. The employed method of calculation for the distribution of the electric field intensity, as shown in Fig, 1, is detailed in the following section.

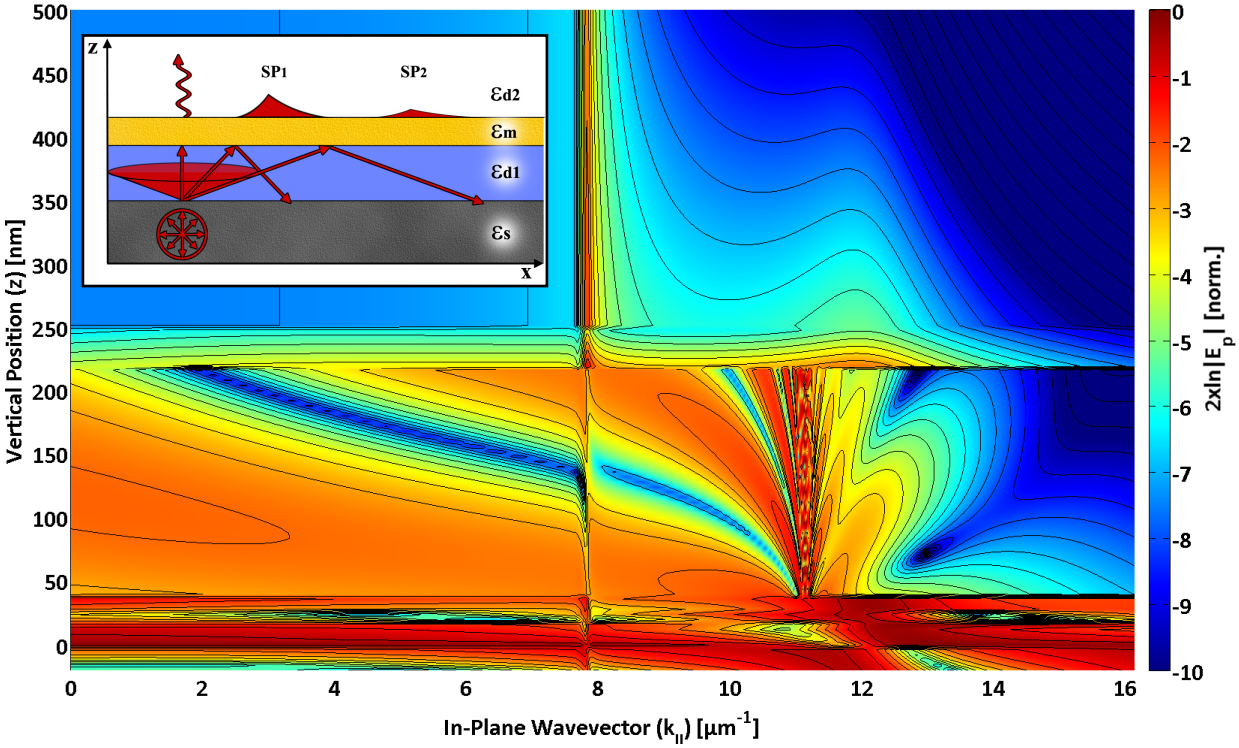

Fig. 1. **Inset:** The embedded semiconductor (ε_s) emits an uncollimated and usually incoherent light. At fixed energy, the DMD interface (ε_{d2} - ε_m - ε_{d1}) is exposed to a continuous range of wavevector excitation, coupling all the SPR modes possibly supported by the architecture. Since the whole semiconductor layer (ε_s) emits in the depicted manner, a constant light intensity is measured in the real space, while all photonic modes can be excited in the Fourier space (k_{ll}). If the light source emits a broad energy spectrum, a continuum of dispersion relations $\omega(k_{ll})$ can be met. **Main**: Distribution of the P-polarized electric field intensity in logarithmic scale for various vertical positions of the architecture (z) in the near field at various emitted in-plane wavevectors (k_{ll}) for 1.51eV light emissions. The architecture is a GaAs-AlGaAs QW heterostructure with a SiO2-Au-Air DMD as presented in previous work[2]. Note the two SPR events occurring concurrently (past their respective TIR).

The embedded semiconductor light sources will have a relatively large emission spectra (from ±50-nm in QW to ±100-nm in NCs), thus they will simultaneously generate a continuum of SPs dispersion relation $\omega(k_{ll})$ (angular frequency versus in-plane wavevectors). This case is different from the traditional "macro" SPs coupling, where one energy is considered and one wavevector is injected by the irradiating laser [1, 3].

We have already reported on the measurements of SP effects in a DMD microstructure comprising SiO_2–Au deposited on top of a PL emitting GaAs-$Al_{0.5}Ga_{0.5}As$ QW microstructures[2]. The extraction of SPs in these microstructures was achieved with a short-period grating fabricated within the Au layer. However, only a semi-qualitative interpretation of the results could be provided due to the lack of an analytical tool capable of predicting the full behaviour of the observed effects. In this communication, we discuss details of our calculations aimed at the description of SPs generated in DMD microstructures monolithically interfaced with self-emitting semiconductor architectures. We also discuss an architecture optimized for the observation of the SPR effect, where we achieved the increase in S/N up to 10^3 times. Moreover, we introduce an innovative method for the characterization of light emitting SPR devices, which takes advantage of the hyperspectral imaging technology.

Downloaded from SPIE Digital Library on 17 Jun 2010 to 132.210.72.142. Terms of Use: http://spiedl.org/terms

2. SEMICONDUCTOR LIGHT SOURCES FOR SPR

The calculations were carried out using a Rigorous Coupled-Wave Analysis (RCWA) algorithm that we upscaled with tensor algebra. The method consists in dividing any investigated architecture in a set of layers. Grating profiles functions, ex: f(z,x) in 1D, are approximated by a subset of rectangular layers and the reflected and transmitted fields in the regions above and beneath are a superposition of diffracted plane waves as illustrated in Fig. 2 and within literature[4, 5].

No approximations are used for material properties or in the case of square gratings and layered architectures. The method allowed us to predict the coupling of semiconductor photoluminescence (PL) to SP generating architectures and describe the propagation of SPs in both the Near- and Far-Fields. The RCWA approach was preferred in these cases because it has been shown to be remarkably robust: for arbitrary shapes, it is able to reliably compute the electromagnetic field distribution for any wavelengths and incidence angles [4-6], even for conical diffraction mounting [7]. The studied architectures consist of layered dielectrics, which simplify even further the required calculations by reducing the complexity of the problem, eliminate approximations and designate RCWA as a perfect candidate for analytic solutions. For a given architecture, a set of variables, such as energies, angles, spatial positions (near- and far-fields) or dielectric thicknesses are solved simultaneously through tensor algebra. A 2D or 3D slice of the solution, such as near-field spatial distribution or a dispersion relation map $\omega(k_{ll})$, can then be presented in the form of a plot. This tensorial approach generates an efficient design tool to address specific targets in photonic or biochemical responses as well as the optimization of existing architectures. All the calculations are done using a standard PC (Intel® Core Duo™ CPU, 2.33 GHz, 1.95 GB RAM) using MATLAB® language. The gratings presented are considered semi-infinite over the specified dimension as the sample ($1cm^2$) and grating regions ($1mm^2$) are much larger than the employed wavelengths (IR) and SPs propagation lengths (μm scales). The computation time of the method is also attractive, with the allotted time for the solution of the inverse problem typically between 2 and 10 seconds (solver and hardware dependent).

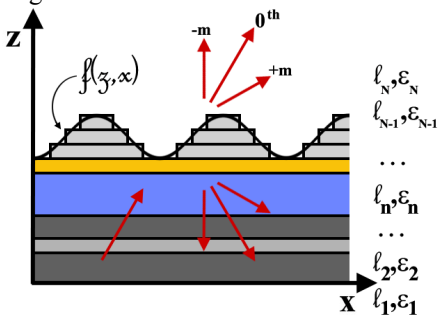

Fig. 2. Architectures are divided in a series of N layers of dielectric value ε_n. Geometrically patterned periodic regions f(z,x) are discretized into subsets of N' square gratings layers. The reflected and transmitted EM field can thus be calculated by superposing the diffraction orders m (with m an integer) anywhere in space. Tensor algebra allows extending the calculations to multiple variables such as sets of energies, wavevectors, etc. The differences in diffraction output between the profiles functions f(z,x) and the discrete approximation of N' square gratings rapidly converges with N' or is zero for square gratings and flat layers [4, 5].

We have previously reported the verification of the developed analytical tools for various microstructures[8]. For example, Fig. 3 presents the calculated dispersion relation $\omega(k_{ll})$ for a silicon nanocrystals (Si-NCs) architecture as diffracted in the far-field by a photoresist (PR) grating[9]. Only the 1st diffraction order is presented for clarity. The spectrum is modulated by the Si-NCs PL emission. The white dots are the local maxima experimentally measured in the original paper[9]. Up to a 10% error should be added to these results from the NA of the setup (inducing a $\pm 1^o$ uncertainty). The dashed lines follow the calculated local maxima for the surface plasmon polaritons (SPP) resonance modes (for both the Au/ Si-NCs and Au/PR interfaces). As presented on Fig. 3, the calculations are in very good agreement with the experiment. Here, the analytical predictions are in better agreement than originally presented [9] because the SPR is not the only effect taken into account in our calculations of the far-field intensity distribution. Sums of other phenomena, such as the architecture's transmittance, the guided modes and the photonic bandgaps are taken into account in our analytical approach. This has allowed us to predict more rigorously the experimental values of PL peak intensities. Other calculations also included the accurate prediction of the collected far-field emissions from a GaAs-AlGaAs QW heterostructure inducing SPR modes on a SiO_2-Au-Photoresist (PR) monolithic structure[2,8]. In the later configuration, a very strong SPs coupling was observed within the architecture. This is caused by the nature of the semiconductor material, as will now be exposed.

Downloaded from SPIE Digital Library on 17 Jun 2010 to 132.210.72.142. Terms of Use: http://spiedl.org/terms

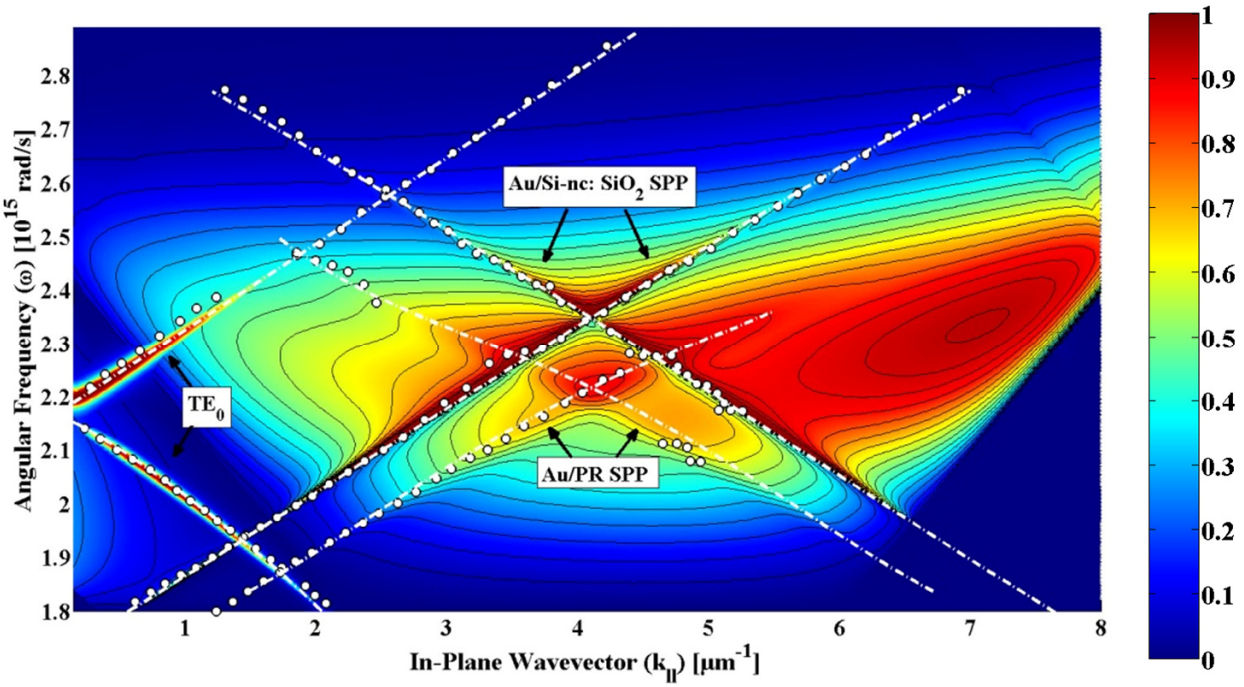

Fig. 3. Calculated dispersion relation $\omega(k_{ll})$ of the Si-NCs architecture in the 1st diffraction order as observed in the far-field[8]. White lines follow the analytical SPR peaks from the Au/ Si-NCs SPP, the Au/ PR SPs and the TE_0 mode. White dots are experimental results from the literature[9]. The intensity is modulated by the Si-NCs emission and normalized to one.

3. GRATING DIFFRACTION AND SURFACE PLASMON COUPLING

At a given metal-dielectric interface, SPs always have a greater in-plane wavevector than free propagating light in the medium ($k_{SP} \geq k_{ll}$)[3], thus the use of a prism is required in classical configurations to couple SPs. When using monolithically integrated light emitting semiconductor structures, there is no mechanical scan of the polar angle of incidence: all in-plane wavevectors are emitted concurrently by the source, with $-k_0\varepsilon_{Source} \leq k_{ll} \leq k_0\varepsilon_{Source}$ ($k_0 \equiv 2\pi/\lambda_{Source}$), as illustrated in Fig. 1.

As previously covered[8], no SPs can be coupled in the 0th diffraction order for the Si-NCs setup presented in Fig. 3. In other words, no SPR is supported by this architecture without the grating. This is because the maximum in-plane wavevector (k_{ll}) emitted by the integrated source (Si-NCs) can never meet the SPs wavevectors (k_{SP}) at the Au/Si-NCs or Au/PR interfaces ($k_{SP2} > k_{SP1} > k_0\varepsilon_{Source}$). Clearly, the SPs can only couple through the diffraction where $k_{SP} = k_{ll} \pm n.k_G$ can be met ($n = \pm1,\pm2$) and the resulting SPs PL intensities are very weak. In the studied GaAs-AlGaAs QW heterostructure, the two SPs modes are coupled in the 0th diffraction order, and also in higher orders, because the k_{ll} from the source can always meet k_{SP} ($k_{SP1} < k_{SP2} < k_0\varepsilon_{Source}$). This is possible because for an uncollimated light source, where any point of the interfaces is exposed to the whole range of wavevector spectra of $k_{ll} \leq k_0\varepsilon_{Source}$, the SPs conditions at the two interfaces can be fulfilled for both the $\pm1^{st}$ and 0th diffraction orders. The resulting S/N ratio, independent of total transmission power, was found to be 100x larger when coupling SPR in the 0th diffraction order, in contrast with diffraction coupling, necessary when $\varepsilon_{d1} < \varepsilon_{d2} < \varepsilon_{Source}$ is not fulfilled.

As demonstrated, coupling through the 0th order always results in stronger PL modulations (for symmetric gratings) and thus, for a given source power and grating structure, the rest of the architecture is left to be optimized for the desired application and measurement system. Fig. 4 presents two cases of 0th order SPR coupling, where the architecture consist of the same GaAs-AlGaAs QW atop of which a SiO_2 – Au – Air/PR DMD is microfabricated. The dashed (blue) curve presents the unoptimized, ad hoc, architecture previously studied[2, 8]. The two extracted SPs are overlapping in one peak and are diffracted far from the normal ($k_{ll} = 0\mu m^{-1}$) through a 20nm thick Au grating. The solid (red) line is the same architecture and dielectrics, where the thicknesses of the various dielectrics were chosen as to maximize the S/N ratio for SP_1. The extraction of the far-field is done with a 55-nm corrugated PR square grating. The periodicity (750-nm) is selected to extract the first SP_1 near normal incidence.

Downloaded from SPIE Digital Library on 17 Jun 2010 to 132.210.72.142. Terms of Use: http://spiedl.org/terms

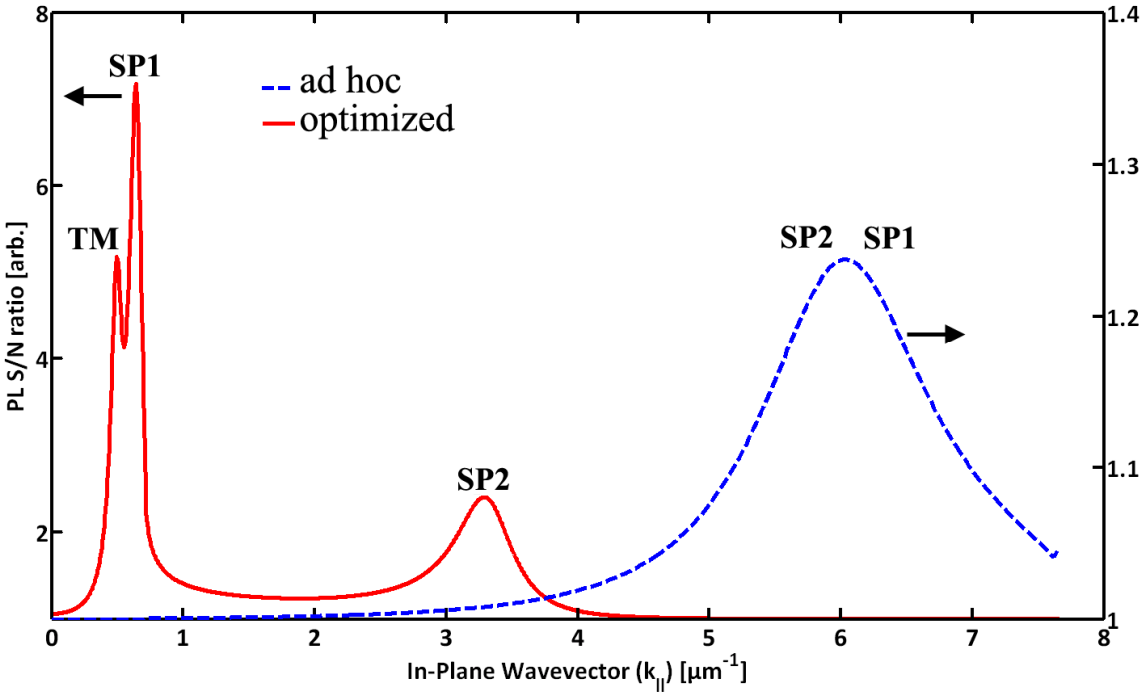

Fig. 4. S/N ratio in total PL for different architectures taken at $\hbar\omega = 1.51$ eV: In dashed blue is the QW setup with $\varepsilon_{Source} > \varepsilon_{d2} \approx \varepsilon_{d1}$ with scale from 1 to 1.4. SP_1 corresponds to the exposed surface (Air or PR) and SP_2 to the enclosed interface (SiO_2). The solid red line presents the case of $\varepsilon_{Source} > \varepsilon_{d2} > \varepsilon_{d1}$ when the architecture is optimized for the extraction of SP_1. Note the scale going from 1 to 8 for this curve, resulting in a 10 times stronger S/N than the dashed blue curve and 10^3 times compared to literature[8, 9].

By optimizing the architecture, we can thus increase the S/N further by a factor of 10, which is 10^3 times stronger than the Si-NCs case. Furthermore, the resulting SP_1 peak sharpness is much greater than the previous device (over 10 times smaller FWHM versus the dashed (blue) line), resulting in a more precise SPR tracking potential. As identified in the graph, the SP_2, from the SiO_2 – Au interface, is still present in the extracted far-field; this could also be employed as an embedded reference as the SP_2 resonance is not perturbed by surficial events. In addition to the two SPR, a TM mode is coupled in the relatively thick 55-nm PR grating layer. This TM mode is also extracted in the far-field in the $\pm$ 1st diffraction orders and behaves very differently than the SPRs as a function of energies and surface events (graphs not presented here).

The drastic difference with the last device mainly comes from the nature of the grating, where the 20-nm Au corrugation was replaced by 55-nm of PR. In the studied architectures, the grated Au layer plays the role of a diffracting element, but it also affects the SPs coupling itself, given the metallic nature of the corrugation[10]. This additionally induces an enlargement of the SPR(k_{ll}) event. A similar, but lesser effect is observed using a thin Au layer overcoating a PR grating. The use of Au corrugation has the advantage of requiring smaller features, due to the high dielectric values of the metal, and might play a role in dynamic surficial events. Au is also a well known and biocompatible material, which positively influences the biochemical reactions under SPR study[1, 11]. Therefore, there should be tradeoffs between using Au corrugations and SPR sensing of biochemical reactions. Theses interactions will be addressed in future studies.

Downloaded from SPIE Digital Library on 17 Jun 2010 to 132.210.72.142. Terms of Use: http://spiedl.org/terms

4. MEASURING UNCOLLIMATED BROADBAND EMISSIONS

There are several advantages in monitoring self-induced SPR through uncollimated emissions, when compared to traditional SPR techniques. For instance, many SPR modes can be coupled simultaneously, generating intrinsic references to the measurements[12]. Moreover, the monolithic integration with semiconductor technology generates a self-aligned, self-referred, ultra-compact and potentially inexpensive SPR platform. When using broadband coupling, as with QW or NCs semiconductor microstructures, SPR can be monitored over ranges of energies for various excitation angles concurrently: generating a full spectroscopic SPR platform. The main drawback of the technology is the sheer amount of information to collect from a single architecture. Specifically, to fully map the far-field emission of a given structure, one needs to map the projected wavevectors k_x and k_y (since $k_{ll}^2 = k_x^2 + k_y^2$) for all the emitted energies $\mathbf{E}(k_0)$. This is extremely strenuous through classical means; for example: in Fig. 3 every data point is the result of a carefully aligned setup, taking hours to adequately monitor, which still result in over $\pm 1^o$ errors. This is completely unacceptable for practical application of the SPR effect in the monitoring of biochemical reactions occurring in the minute scale of time and where angular resolution of the SPR peak has to be monitored with an angular precision of $1x \cdot 10^{-3}$ - $1x \cdot 10^{-6}$ deg for adequate characterizations.

In currently applied SPR experiments, the problem is addressed by reducing the variables: a (monochromatic) laser is sent to a Au-coated prism and the intensity of its reflection measured with a photodiode. The minimum in reflectance (corresponding to the SPR angle) is monitored over time to provide a relative angular shift as biochemical processes are occurring[13]. At one point in time, a single energy is recorded for a fixed k_x and k_y incidence. In efficient systems, the laser is made divergent, a set of k_x are injected at fixed $E(k_0)$ and k_y, and an array of photosensors can record up to 10^3 intensities simultaneously.

Rather than isolating every variables (polar and azimuthal angles, k_x and k_y, and energies) as in literature[8, 9], where several hours could pass between experiments, we take advantage of an hyperspectral imaging method. Do to so, we modified a hyperspectral photoluminescence mapper microscope[14] to effectively monitor the Fourier plane (k_x-k_y space) of the light emitted from the photonic architecture over a broad spectral emission of energies $\mathbf{E}(\mathbf{k_0})$. The sketch of Fig. 5 presents the basic principle of the setup, where the uncollimated emissions from the SPR device are collected and recorded on a CCD.

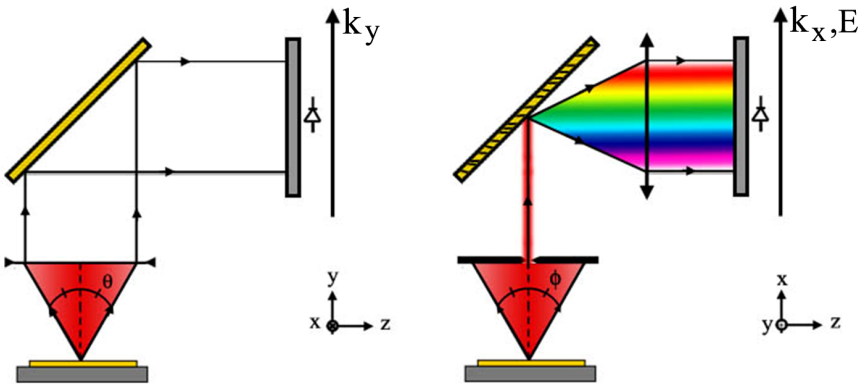

Fig. 5. Basic functioning of the hyperspectral approach: The uncollimated emissions from the architectures are collected for a set of polar and azimuthal angles ($\mathbf{k_x}$ and $\mathbf{k_y}$). The collected beam is sent to a grating which splits the collection into separate emitted energies $\mathbf{E}(\mathbf{k_0})$ monitored by a CCD. A grating scan and a mathematical deconvolution of the collected data allows to construct 3D cubes of the emitted **E(kx, ky)** within very short period of time.

The precision of the $\mathbf{k_{ll}}$ mapping is related to the CCD of the microscope along with the microscope objective (M.O.) employed, where the NA and the magnification dictates the range of monitored E, k_x, k_y and their precision (yielding the angular precision of the SPR tracking). Therefore, the resulting system is extremely flexible given the variety of M.O. available commercially. This allows us to directly track the 3D dispersion relation of the coupled SPs, $\mathbf{E}(\mathbf{k_{ll}}) = \hbar\boldsymbol{\omega}(\mathbf{k_{ll}})$, at a given time, in the form of recorded "cubes" of dispersion relations.

Downloaded from SPIE Digital Library on 17 Jun 2010 to 132.210.72.142. Terms of Use: http://spiedl.org/terms

Where commercial SPR systems monitor 1 to 10^3 elements in parallel[1], our hyperspectral approach allows us to monitor over $320 \cdot 10^6$ elements for a 100nm spectral bandwidth. Therefore, each measurement is the equivalent of 10^5 to 10^8 conventional SPR scans with commercial systems. As in any spectroscopic approach, monitoring biochemical interactions as a function of $\mathbf{E}(\mathbf{k_{II}})$ provides a much richer picture of the nature of the near-field photonic interactions and thus biochemical reactions taking place at the device surface.

Examples of hyperspectral measurements are presented in Fig. 6 where a Nikon CFI Plan Apo 10X is employed, thus averaging the signal over the $1mm^2$ field of view (FoV) with a 360^o azimuthal and 17^o polar ($4.5975 \mu m^{-1}$) emissions monitoring. This non-optimized measurement yields a precision of 10^{-4} RIU for the presented M.O. The initial goal of this experiment is the demonstration of uncollimated broadband emissions measurements, paving the way to 3D $\mathbf{E}(\mathbf{k_{II}})$ biochemical SPR sensing. Therefore, the examined architecture is a GaAs-AlGaAs QW with a SiO_2-Au-PR DMD similar to the one reported earlier[2], but in which the measured far-field diffraction comes from a 20-nm Au line notch. Fig. 6(a) presents the measured light intensity for a map of k_x-k_y, at fixed energy $\hbar\omega = 1.51$ eV. The far-field corresponds to the expected output: a convolution of a 1D sinc signal with the 0^{th} diffraction order (normal transmission). The red dots show the features tracking (only applied over half the image for clarity), which aims at facilitating the analysis and real-time monitoring of future biosensing experiments. Slices of information can also be taken over the energy axis of the collected cube. For example, Fig. 6(b) presents the dispersion relation of the collected far-field, at fixed $k_y = 0\ \mu m^{-1}$. The dispersion of the diffracted elements are clearly visible and again traceable (red dots) for further analysis.

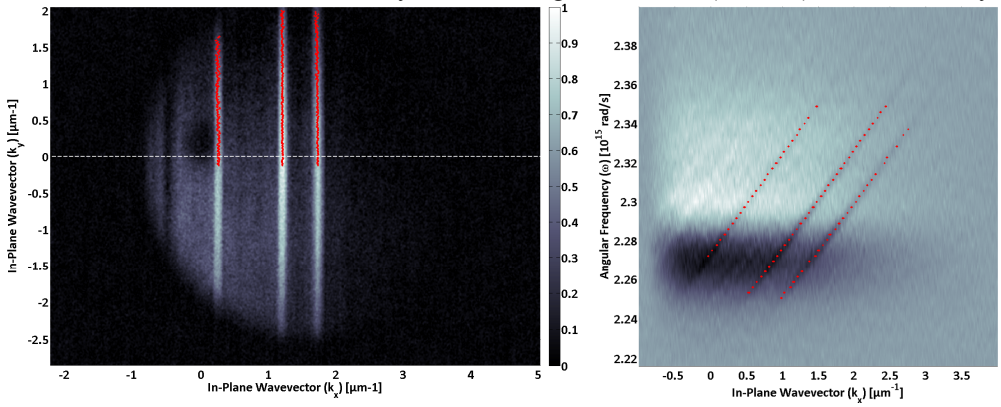

a) **b)**

Fig. 6(a) Measured Far-field intensity for a range of k_x and k_y, at $\hbar\omega = 1.51$ eV. The range and resolution is set by the employed M.O. The observed features correspond to the convolution of a 1D sinc with the background transmission, induced by a 20nm Au diffraction notch. Fig. 6(b) is a cross section of the monitored dispersion relation $\omega(k_x)$, at fixed $k_y = 0\ \mu m^{-1}$. In both graphs, the red dots reflect the possibility to track the features within the collected cubes for analysis and real-time monitoring.

More interestingly, the recorded information is the spectral responses $\mathbf{E}(\mathbf{k_{II}})$ emitted by the whole monitored FoV of the M.O. So, any independent SPR experiments occurring within the selected FoV will simultaneously be recorded by the hyperspectral SPR method. Therefore, the potential number of measurement channels accomplishable in parallel through this method is fixed by the ability to run SPR experiment within the chosen (and adaptable) FoV. This FoV can vary from the µm scale to cm scale in standard commercial M.O. Combined with recent advances in microfluidics and semiconductor microfabrication methods, we believe the proposed method could yield the real-time mass SPR multiplexing response of independent channels.

In conclusion, we have implemented the RCWA algorithm in the form of tensor algebra to provide a detailed description of the formation and propagation of SPs at metal-dielectric microstructures deposited atop light emitting semiconductor substrates. The developed analytical tools have enabled us to predict both the far-field and near-field SP-assisted PL emissions. We also used the tensor approach to optimize and design photonic architectures of specific targeted applications. For symmetric square or sinusoidal gratings, SPs coupling was found to be up to 10^3 times stronger when all SPs are coupled in the 0^{th} diffraction and the architecture S/N output optimized. An excellent agreement has been observed between calculated and measured experimental results. This understanding allowed us to highlight the specific role of semiconductors as light sources for monolithically integrated SPR systems. In addition, a highly novel measurement method has been developed in order to fully take advantage of the SPR coupled through uncollimated emissions of microstructures. Indeed, by adapting hyperspectral imaging methods to SPR microscopy, we

Downloaded from SPIE Digital Library on 17 Jun 2010 to 132.210.72.142. Terms of Use: http://spiedl.org/terms

enabled the monitoring of over $320 \cdot 10^6$ independent far-field photonic responses, which corresponds to an equivalent of 10^5 to 10^8 conventional SPR scans with existing commercial systems. The high quality measurement of biochemical interactions as a function of $\mathbf{E}(\mathbf{k}_{\parallel})$ will provide a drastically richer picture of the surficial events and biosensing. The explicit conditions established for monolithic SPR represent a fundamental step towards designing a fully integrated quantum semiconductor SPR biosensing device. Future work will include the hyperspectral monitoring of SPR events in various conditions and a time-dependent tracking of the 3D dispersion relations for biosensing.

5. ACKNOWLEDGMENTS

The authors acknowledge the financial contribution from the Natural Science and Engineering Research Council (NSRC) of Canada (Strategic grant STPGP 350501 - 07) and the Canada Research Chair in Quantum Semiconductors Program (JJD). Dominic Lepage is an NSERC Vanier Graduate Student Scholarship holder.

6. REFERENCES

[1] R. B. M. Schasfoort, and A. J. Tudos, [Handbook of surface plasmon resonance] Royal Society of Chemistry, Cambridge(2008).

[2] D. Lepage, and J. J. Dubowski, "Surface plasmon assisted photoluminescence in GaAs-AlGaAs quantum well microstructures," Applied Physics Letters, 91, (2007).

[3] H. Raether, "Surface-Plasmons on smooth and rough surfaces and on gratings," Springer Tracts in Modern Physics, 111, 1-133 (1988).

[4] L. F. Li, "Fourier modal method for crossed anisotropic gratings with arbitrary permittivity and permeability tensors," Journal of Optics a-Pure and Applied Optics, 5(4), PII S1464-4258(03)60323-5 (2003).

[5] M. G. Moharam, D. A. Pommet, E. B. Grann *et al.*, "Stable implementation of the rigorous coupled-wave analysis for surface-relief gratings-enhanced transmittance matrix approach," Journal of the Optical Society of America a-Optics Image Science and Vision, 12(5), 1077-1086 (1995).

[6] J. Hench, and Z. Strakos, " *The RCWA method - a case study with open questions and perspectives of algebraic computations*," to appear in ETNA, (2009).

[7] L. Mashev, and E. Popov, "Reflection gratings in conical diffraction mounting," Journal of Optics-Nouvelle Revue D Optique, 18(1), 3-7 (1987).

[8] D. Lepage, and J. J. Dubowski, "Surface plasmon effects induced by uncollimated emission of semiconductor microstructures," Opt. Express, 17(12), 10411-10418 (2009).

[9] E. Takeda, T. Nakamura, M. Fujii *et al.*, "Surface plasmon polariton mediated photoluminescence from excitons in silicon nanocrystals," Applied Physics Letters, 89(10), (2006).

[10] T. Okamoto, J. Simonen, and S. Kawata, "Plasmonic band gaps of structured metallic thin films evaluated for a surface plasmon laser using the coupled-wave approach," Physical Review B (Condensed Matter and Materials Physics), 77(11), 115425 (2008).

[11] J. C. Love, L. A. Estroff, J. K. Kriebel *et al.*, "Self-Assembled Monolayers of Thiolates on Metals as a Form of Nanotechnology," Chemical Reviews, 105(4), 1103-1170 (2005).

[12] S. Patskovsky, A. V. Kabashin, M. Meunier *et al.*, "Silicon-Based Surface Plasmon Resonance Sensing with Two Surface Plasmon Polariton Modes," Appl. Opt., 42(34), 6905-6909 (2003).

[13] NanoSPR, [www.nanospr.com], (2009).

[14] Photonetc, [www.photonetc.com], (2009).

Downloaded from SPIE Digital Library on 17 Jun 2010 to 132.210.72.142. Terms of Use: http://spiedl.org/terms